nanomaterials

MDPI

Article

Ag–Se/Nylon Nanocomposites Grown by Template-Engaged Reaction: Microstructures, Composition, and Optical Properties

Valentina Krylova *, Nijolė Dukštienė and Henrieta Markevičiūtė

Department of Physical and Inorganic Chemistry, Faculty of Chemical Technology, Kaunas University of Technology, Radvilėnų Str. 19, 50254 Kaunas, Lithuania; nijole.dukstiene@ktu.lt (N.D.); henrieta.markeviciute@ktu.edu (H.M.)

* Correspondence: valentina.krylova@ktu.lt

Abstract: Ag–Se nanostructure films were deposited on a–Se/nylon templates by a template-engaged reaction. Firstly, amorphous selenium (a–Se) was deposited on nylon by employing the chemical bath deposition method while using H_2SeO_3 and Na_2SO_3 solutions with an increasing selenium deposition time. Then, these a–Se/nylon templates were exposed into $AgNO_3$ solution at ambient temperature and pressure. The Ag–Se/nylon nanocomposites surface morphology, elemental and phase composition, and optical properties were monitored depending on the selenium deposition time on nylon. Scanning electron microscopy (SEM) analysis confirmed the development of a very complex surface composed of pyramidal-like sub-micron structures, agglomerates, and grid-like structures. Energy dispersive spectroscopy (EDS) proved the presence of carbon, oxygen, nitrogen, selenium, and silver. SEM/EDS cross-sectional analysis confirmed the multilayer character with different individual elemental composition in each film layer. X-ray diffraction analysis revealed a polycrystalline Ag_2Se phase with or without metallic Ag. The RMS value obtained from atomic force microscopy varies from 25.82 nm to 57.04 nm. From the UV-Vis spectrophotometry, the direct optical band gaps were found to be 1.68–1.86 eV. Ag–Se/nylon composites exhibit high refractive indices in the near infrared region.

Keywords: Ag_2Se; nylon 6; flexible inorganic-organic composite; ProX-SEM-EDS; optical properties

check for updates

Citation: Krylova, V.; Dukštienė, N.; Markevičiūtė, H. Ag–Se/Nylon Nanocomposites Grown by Template-Engaged Reaction: Microstructures, Composition, and Optical Properties. *Nanomaterials* **2022**, *12*, 2584. https://doi.org/10.3390/nano12152584

Academic Editors: Jihoon Lee and Ming-Yu Li

Received: 22 June 2022
Accepted: 25 July 2022
Published: 27 July 2022

Publisher's Note: MDPI stays neutral with regard to jurisdictional claims in published maps and institutional affiliations.

Copyright: © 2022 by the authors. Licensee MDPI, Basel, Switzerland. This article is an open access article distributed under the terms and conditions of the Creative Commons Attribution (CC BY) license (https://creativecommons.org/licenses/by/4.0/).

1. Introduction

Currently, a lot of attention is devoted to the flexible photovoltaic membranes, as they can maintain the required durability and fulfil the aesthetic, building-physics requirement(s) [1]. Therefore, the demand for a sustainable and semi-permanent energy-harvesting system, which converts solar energy to electricity, has been continuously increasing. Photovoltaic devices also need to be mechanically flexible to be employed as an energy supplier for a curved electronic device. Hybrid organic–inorganic composites are considered as very attractive and promising materials due to the diverse properties and additional functionalities as compared with those of individual components [2]. Thin films of solar light absorbers such as metal chalcogenides are of extraordinary interest for the production of solar selective coatings, large area arrays, and photovoltaic cells. The modification of flexible polymers with metal chalcogenides not only allows control an architecture of resultant solar absorbers, but also enables the creation of flexible materials with the unique microstructures and optical properties. Printing and coating methods are two main techniques to deposit thin films onto the flexible polymer surface [1]. Recently, surface modification of organic polymers with metal chalcogenides thin films via different coating techniques have been reported [3].

Owning to its high mechanical strength and high chemical and thermal stability, nylon 6 (polyamide 6) is a promising candidate for high-performance flexible energy-harvesting systems. Among a variety of metal chalcogenides, silver selenide displays many interesting

properties. Ag_2Se exists in two polymorphs at atmospheric pressure: a low-temperature orthorhombic phase (α-Ag_2Se), and a high-temperature cubic phase (β-Ag_2Se) [4]. β-Ag_2Se is distinguished for its Seebeck coefficient (-150 μ VK^{-1} at 300 K [5]), large magnetoresistance [6], and excellent thermoelectric properties [7]. The Ag_2Se nanowires phase nature greatly influences electrical conductivity [8]. Authors [9] stated a super-ionic α-Ag_2Se conductor was employed in photo chargeable batteries. Environmentally friendly, an n-type nanocrystalline, Ag_2Se thin film exhibits the direct bandgap of 1.8 eV [10].

From the broad list of available literature, only a few articles have reported that a facile strategy has been developed to prepare flexible Ag_2Se films and Ag_2Se-based composite films on nylon [7,11,12]. These multiscale Ag_2Se nanoparticles with or without Ag nanoparticles on nylon exhibit a high power factor and excellent flexibility [7,12]. Through literature analysis, we did not succeed in finding any publication devoted to optical properties of Ag_2Se/nylon composites. Considering the rapid application of hybrid materials in opto-electronic modules, such study remains relevant, significant, and timely.

Template-assisted synthesis represents a straightforward, adaptable, and successful nanomaterial synthesis approach. In this approach, the templates may serve as physical scaffolds, against which other materials are assembled, or templates are engaged in synthesis as one of the reactants (template-engaged reactions). Recently, several teams have described the synthesis of Ag_2Se nanotubes [13,14], nanowires [5,15], and Se/Ag_2Se/core/shell nanocables [14] by this technique. The authors emphasised that the resulting Ag_2Se have retained the both shape and morphology of trigonal Se template with good precision.

In this study, compact Ag–Se/nylon semiconductor nanocomposites were formed via a template-engaged reaction, which could convert the amorphous selenium (a–Se) layer on nylon into an Ag–Se film. The sequential deposition method was explored. The type of the template, as well as its amount, exerts a strong influence on the structure and the properties of the resulting composites. Firstly, a–Se was deposited on nylon 6 while using the chemical bath deposition (CBD) method by mixing solutions of H_2SeO_3 and Na_2SO_3 and changing the time of selenium deposition. These a–Se/nylon templates were then exposed to the $AgNO_3$ solution. The Ag–Se/nylon nanocomposites surface morphology, elemental and phase composition, and optical properties were monitored depending on the selenium deposition time on nylon. The results were interpreted, discussed, and compared with some of the currently available state-of-the-art reports.

2. Materials and Methods

2.1. Polymer

The thermoplastic matrix which we used was semi crystalline nylon 6 *Tecamid 6*, (hereinafter referred as 'nylon') produced by Ensinger GmbH (Germany). The 500 μm-thick nylon film was opaque. The density was 1.13 g/cm^3, moisture absorption 3%, water absorption to equilibrium 9.5%. The experiments were performed on strips of 2′ 6 cm^2 in size. Prior to the experiments, nylon film cuts were washed with Na_2CO_3, and afterward treated in distilled water at 100 °C for 2 h. The criterion for the quality treatment of the nylon substrate surface was its uniform wetting with distilled water. After treatment, the substrates were stored in a desiccator.

2.2. Chemicals

The distilled water and as received analytical grade reagents were used to prepare freshly solutions for each experiment. Selenous acid (H_2SeO_3, 99.0%) and sodium sulphite heptahydrate ($Na_2SO_3 \cdot 7H_2O$, 99.0%) were obtained from Reachim, Russia. Sulphur acid (H_2SO_4, 96.0%), silver nitrate ($AgNO_3$, 99.0%), and sodium carbonate hydrate ($Na_2CO_3 \cdot 10H_2O$, ≥99.0% (calc. based on dry substance)) were purchased from Aldrich Chemical Co.

2.3. Sample Preparation and Theoretical Background

The first step involved the formation of a selenium film via the CBD method. The concentrations of H_2SeO_3 and Na_2SO_3 solutions and temperature that yielded a superior a–Se/nylon template, with respect to continuity, smoothness, and the adherence of the selenium film to the substrate, were chosen for further experiments. For Se film deposition, nylon strips were exposed in 0.1 M H_2SeO_3 and 0.15 M Na_2SO_3 solution (pH 2 adjusted with H_2SO_4) for 6, 12, 24, and 30 h at 20 ± 1 °C. The red amorphous selenium (a–Se) isolated according to the following equation [16,17]:

$$H_2SeO_{3(aq)} + 2Na_2SO_{3(aq)} \rightarrow Se_{(s)} + 2Na_2SO_{4(aq)} + H_2O. \quad (1)$$

The half reactions for the reduction and oxidation of selenous acid and the sulphite ion, respectively, are the following Equations (2) and (3):

$$H_2SeO_{3(aq)} + 4H^+_{(aq)} + 4e^- \rightarrow Se_{(s)} + 3H_2O, \quad (2)$$

$$SO_3{}^{2-}{}_{(aq)} + H_2O - 2e^- \rightarrow SO_4{}^{2-}{}_{(aq)} + 2H^+_{(aq)}. \quad (3)$$

The reduction potentials ($E^0{}_{red}$) are 0.74 V for Equation (2) and 0.17 V for Equation (3), respectively. Therefore, sodium sulphite reduces selenite readily, and the redox reaction is spontaneous [16].

For Equation (1), an acidic environment and the stoichiometry of the initial reacting materials are essential in order to prevent the formation of polythionates. Monoselenotrithionic acid forms with an excess of H_2SO_3 solution are added to the solution of H_2SeO_3 with ratio 3:1 [17]:

$$H_2SeO_{3(aq)} + 3H_2SO_{3(aq)} \rightarrow H_2SeS_2O_{6(aq)} + H_2SO_{4(aq)} + 2H_2O. \quad (4)$$

Diselenotetrathionic acid forms when H_2SO_3 solution is added to an excess of H_2SeO_3 [17]:

$$2H_2SeO_{3(aq)} + 5H_2SO_{3(aq)} \rightarrow H_2Se_2S_2O_{6(aq)} + 3H_2SO_{4(aq)} + 3H_2O. \quad (5)$$

In an acidic solution, polythionic acids decompose with the release of elemental selenium. Selenotritithionic acid $H_2SeS_2O_6$ is more stable than diselenothionic acid $H_2Se_2SO_6$, which decomposes with the release of elemental selenium at room temperature [17].

Afterward the selenium deposition, the a–Se/nylon samples were cleaned with C_2H_5OH to remove a poorly adhering film. Then a–Se/nylon samples were thoroughly washed with hot distilled water, and, between the subsequent processing steps, were stored in a desiccator. During the second stage, these a–Se/nylon templates were treated for 2 h with 0.1 M solution of $AgNO_3$ (pH 6.35) at 20 ± 1 °C temperature in a thermostatic vessel.

The solid phase formation at the template/solution interface is a dynamic non-equilibrium process requiring careful consideration of the physicochemical pathways by which they proceed. The solubility of the starting material is the determining indicator for the thermodynamic reaction feasibility in thin films deposition. The change in system Gibbs free energy is also determinant in the solid-state reaction pathway [18,19]. Additionally, the ion-exchange reactions can precede through simple mutual diffusion [20]. The highly reactive elemental Se is an excellent template for the synthesis of various metal selenides even at ambient temperature [5]. If wet films of silver and selenium are stocked together, the reaction–diffusion process starts to yield the silver selenide [21,22]. The formation of Ag_2Se phases in the Ag–Se/nylon nanocomposite could be explained through complex mechanism reactions. When refluxed in an aqueous medium containing Ag^+ cations, amorphous selenium disproportionates into Se^{2-} and $SeO_3{}^{2-}$ anions:

$$3Se_{(s)} + 3H_2O \rightarrow 2Se^{2-}{}_{(ad)} + H_2SeO_{3(ad)} + 4H^+_{(aq)}. \quad (6)$$

Ag^+ ions react with adsorbed chalcogenides particles (Se^{2-}, $SeO_3{}^{2-}$) to generate insoluble nanoparticles, which are in situ deposited on the a–Se/nylon template to produce

Ag–Se/nylon nanocomposites. The major reaction describing Ag_2Se formation can be written as follows [5]:

$$3Se_{(s)} + 6AgNO_{3(aq)} + 3H_2O \rightarrow 2Ag_2Se_{(s)} + Ag_2SeO_{3(s)} + 6HNO_{3(aq)}. \quad (7)$$

As the hydrophilic nylon is treated in the acidified selenium precursor solution, SO_3^{2-}, SO_4^{2-}, and SeO_3^{2-} ions can diffuse into the sub-surface space of nylon, and potentially bind to the charged sites of nylon, such as the ionised functional groups −CONH and –NH [23]. Ag^+ cations could diffuse into the a–Se/nylon template, and the formation of a sub-product within the template matrix—such as Ag_2SO_4, Ag_2SO_3, and Ag_2SeO_3—is probable.

The formed Ag–Se/nylon nanocomposites were thoroughly rinsed with hot distilled water, dried and stored in the desiccator over $CaCl_2$. Throughout the text, the obtained nanocomposites were labelled as Ag–Se-6/nylon, Ag–Se-12/nylon, Ag–Se-24/nylon and Ag–Se-30/nylon, where the added number refers to the selenium deposition time.

2.4. Testing Procedures

The solution pH was measured by using a pH-meter WTW330 (Xylem Analytics Germany Sales GmbH & Co. KG WTW, Weilheim, Germany). An optical microscope CX31 equipped with a C-5050 photo camera (Olympus Corporation, Tokyo, Japan) was used to take the images of uncoated nylon and the obtained Ag–Se/nylon composites. The X-ray diffraction (XRD) analysis was performed on a Bruker Advance D8 diffractometer with Bruker LynxEye counting detector. The operating parameters were the tube voltage of 40 kV, and the tube (emission) current of 40 mA. A Ni 0.02 mm filter selected CuKα (λ = 0.154178 nm) radiation. XRD patterns collected 2θ = 30–70° at a scanning rate of 1° min^{-1} by using the coupled two theta/theta scan type. Scanning electron microscopy coupled with energy-dispersive X-ray spectroscopy (EDS/SEM) analyses were conducted using a Phenom ProX desktop scanning electron microscope (LOT-QuantumDesign) with a high sensitivity multi-mode backscatter electron (BSE) detector. Resolution was ≤8 nm. Primary-beam energy was 0.15 kV EHT. Atomic force a NanoWizard®3 NanoScience microscope (JPK Instruments, Bruker Nano GmbH, Berlin, Germany) with pyramidal-shaped i-type silicon cantilever (0.01–0.025 ohm/cm, spring constant of 2 N/m) operated in the contact mode. The AFM images scanning area was 30 × 30 μm^2. Topographical parameters were evaluated using JPKSPM Data Processing software (Version spm-4.3.13). The diffuse reflectance spectra of the composites were recorded by using a UV-Vis spectrophotometer Lambda 35 within the range 380–1100 nm. The reflectance data were analysed applying the Kubelka Munk model [24–26].

3. Results

3.1. Optical Microscopy and ProX-SEM-EDS *Analysis*

The optical images of the uncoated nylon and corresponding Ag–Se/nylon nanocomposites are shown in Figure 1. The obtained Ag–Se/nylon nanocomposites were homogeneous, spectacularly reflecting with good adherence.

The SEM analysis (Figure 2) indicated that the progression of surface morphology changes is significantly dependent on the selenium deposition time.

As it can be seen, uncoated nylon showed fine dispersion and compact surface morphology. Different small pinholes, bumps, as well as some traces of cracking were visible on the top surface. The surface area of Ag–Se/nylon nanocomposites became larger due to the unevenness and multiple roughnesses, which can be considered as a major source of energy absorption. The surface morphology of Ag–Se-6/nylon sample contained various roads (average size 1.5–4 μm) and irregularly shaped pyramidal-like sub-micron structures (average size 0.5–1 μm). It must also be noted that these units were stacked on top of each other, indicating different stages of growth.

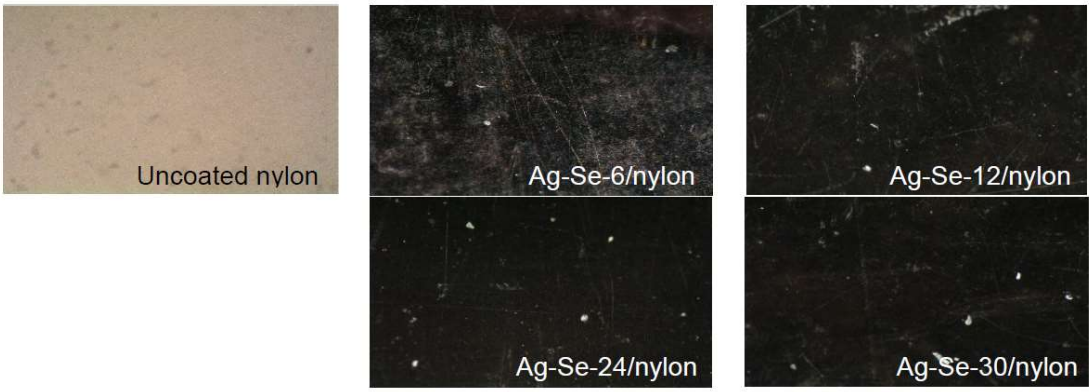

Figure 1. An image of uncoated nylon and obtained Ag–Se/nylon nanocomposites. Magnification 100×.

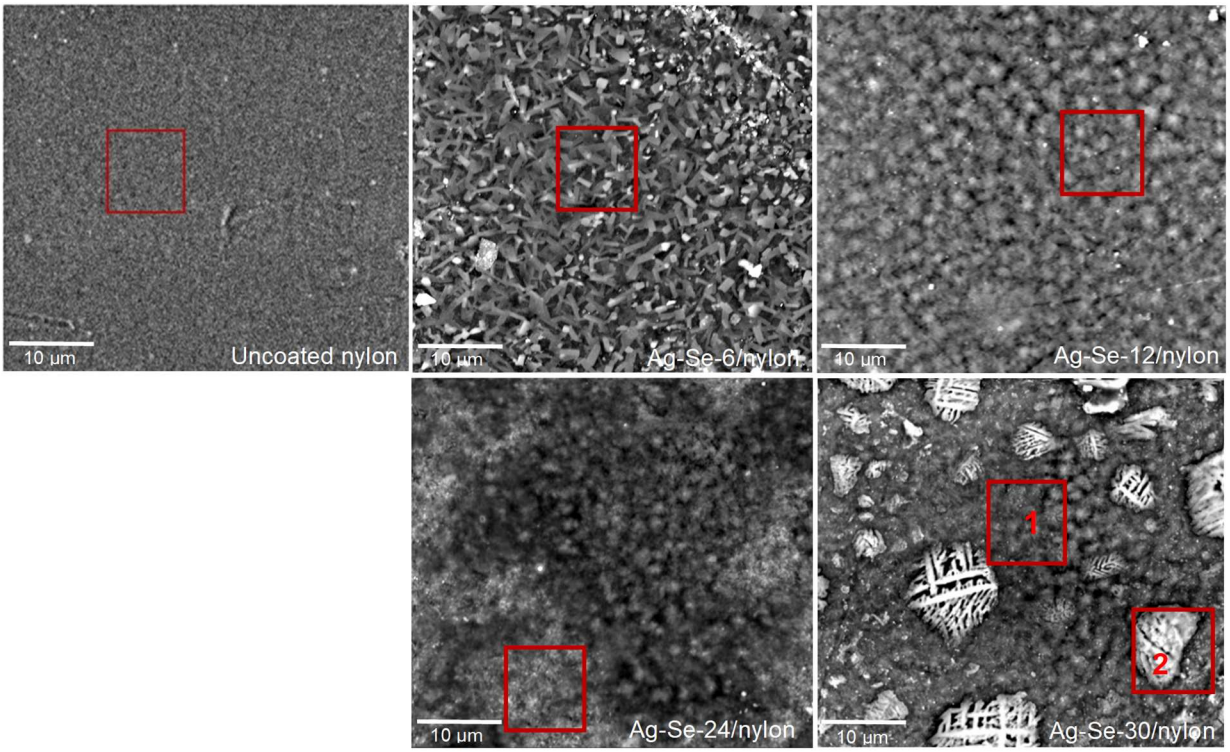

Figure 2. SEM microphotographs of uncoated nylon and Ag–Se/nylon samples with the marked area where the elemental composition was determined by Phenom ProX-SEM-EDS.

The elemental composition from SEM-EDS analysis of a large area (10 × 11.5 µm^2) of an Ag–Se-6/nylon sample confirmed the presence of carbon (C), oxygen (O), nitrogen (N), selenium (Se), sulphur (S), and silver (Ag) (Table 1). The ratio of the Ag/Se atomic concentrations f was 1.24, and it confirmed the overall deficiency of the silver. By increasing the selenium deposition time up to 12 h, we observed an orderly array of tightly packed spherical-like structures. The average diameter of these spherical-like structures was about 3–4 µm. Detailed analysis of the micrograph shows that these spherical-like structures in fact were clumped in various sized clusters. The dark spots are due to the pits in the surface. A similar surface morphology was also visible in the case of the Ag–Se-24/nylon sample. The different clusters of various spherical particles were formed. In addition, the more heterogeneous surface morphology is evident when compared with the Ag–Se-12/nylon sample. There were deeper (darker) areas, and, above them, there were brighter areas consisting of small >0.5 µm derivatives. As expected, Phenom ProX-SEM-EDS spectra from the Ag–Se-12/nylon and Ag–Se-24/nylon samples (Table 1) confirmed that silver, selenium, and sulphur were present in higher concentrations compared with the values of the Ag–Se-

6/nylon sample (Table 1). The ratios of f were 1.81 and 1.34 for the Ag–Se-12/nylon and Ag–Se-24/nylon samples, respectively. With a further increase in the selenium deposition time up to 30 h, significant changes in the Ag–Se-30/nylon sample surface morphology could be discerned. The varying size grains, which created different small granular islands, are visible. Various grid-like structures of irregular shapes in the size of 1–15 µm were randomly arranged on the top-surface of these granules. Granular morphology exhibited f = 2.03 (Table 1, Ag–Se-30/nylon sample area 1), while, for the grid-like structures, f was 2.29 (Table 1, Ag–Se-30/nylon sample area 2). The ProX-SEM-EDS spectra analysis pointed out that not only Ag_2Se nanoparticles, but also Ag was clearly concentrated on the grid-like structures. Metallic silver is the most likely impurity in the chemical deposition of Ag_2Se films [5]:

$$Se_{(s)} + 4AgNO_{3(aq)} + 3H_2O \rightarrow 4Ag_{(s)} + H_2SeO_{3(aq)} + 4HNO_{3(aq)}. \quad (8)$$

As discussed in ref. [27], excess of Ag may be incorporated in various ways: as point defects, as adsorbed metal chains, or as three-dimensional nano- or microscale inhomogeneities. The silver-rich Ag_2Se films exhibit the both negative and linear positive magnetoresistance effects [7,28], and no saturating magnetoresistance [7], which predestines them for various applications.

Table 1. Elemental composition of the Ag–Se/nylon nanocomposites obtained by EDS acquired from the surface area marked in Figure 2.

Sample	Atomic Concentrations, %						
	C	O	N	S	Se	Ag	Ag/Se Concentration Ratio
Uncoated nylon	28.68	44.96	26.36	-	-	-	-
Ag–Se-6/nylon	27.62	52.53	17.31	0.32	0.99	1.23	1.24
Ag–Se-12/nylon	25.14	52.70	17.22	0.90	1.44	2.60	1.81
Ag–Se-24/nylon	29.32	50.05	15.65	1.03	1.69	2.26	1.34
Ag–Se-30/nylon							
area 1	27.76	49.42	17.40	0.93	1.48	3.01	2.03
area 2	31.51	44.50	18.34	0.81	1.47	3.37	2.29

Extraneous elements C and N came from the nylon matrix since it is the largest part of the Ag–Se/nylon samples (Table 1). The higher content of oxygen observed in all the obtained samples as compared with that of the uncoated nylon sample distinctly supports the penetration of oxygen-containing ions, such as SeO_3^{2-}, SO_3^{2-}, or SO_4^{2-}. Although SEM/EDS is useful for the identification of the elemental distribution in micro-domains, however, it must still be appreciated that the elemental information obtained from the micron region is naturally of a heterogeneous nature when compared with bulk analyses.

As discussed above, hydrophilic nylon absorbs various ions from aqueous electrolyte solutions. To collect the relevant information, the cross-sectional analysis was performed, and the representative results are shown in Figure 3.

Three different layers with varying fractional thickness (Table 2) can be clearly identified from the cross-sectional micrographs of Ag–Se/nylon samples. The boundary between each layer is well defined: a highly dense component depicting a homogeneous diffusion layer (grey), an intermediate layer (white), which seems to be composed of coalescence particles, and, finally, the topmost (dark) layer.

The fractional thickness of the topmost layer increased with the selenium deposition time (Table 2), while the fractional thickness of the intermediate layer decreased. The fractional thickness of the diffusion layer showed a non-monotonic character. The total thickness increased with an increase of the selenium deposition time (Table 2). As an example, it was in the range of 22.83–32.33 and 27.1–39.91 µm for Ag–Se-6/nylon and Ag–Se-30/nylon, respectively. EDS analysis was performed to investigate the chemical

composition from each fractional layer of the nanocomposite, and the resulting data (spot 1, spot 2 and spot 3, as marked in Figure 3) are presented in Tables 3–6, respectively.

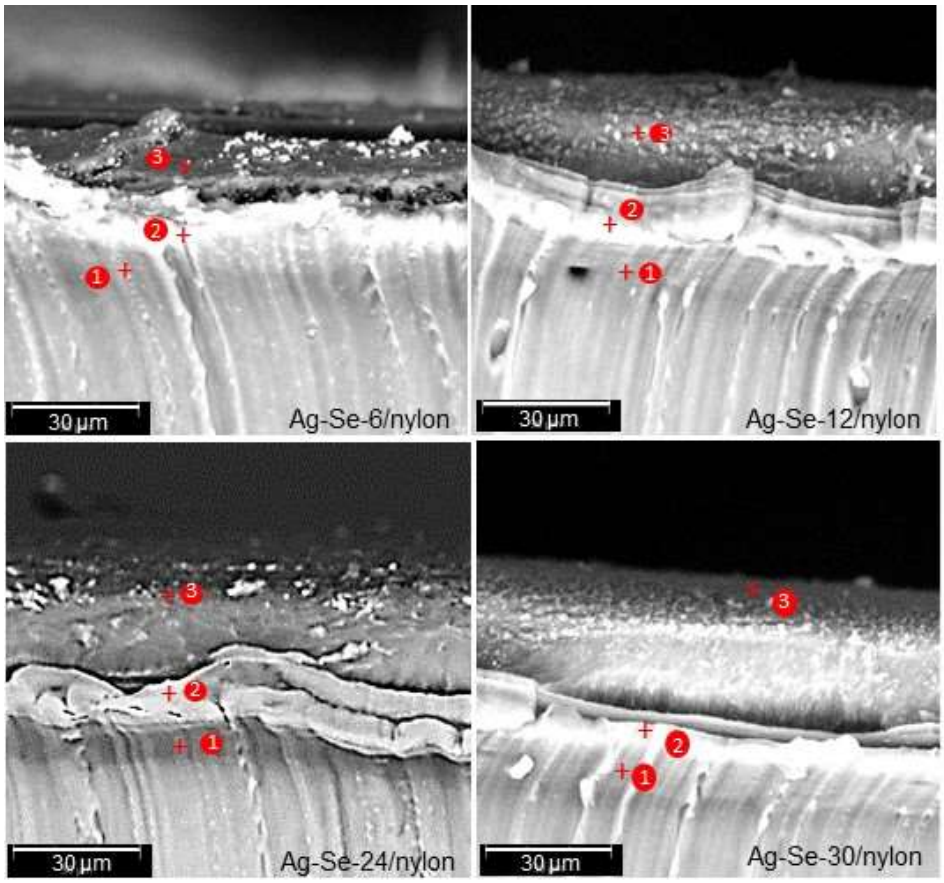

Figure 3. Cross-sectional micrographs of Ag–Se/nylon samples with marked points where the elemental composition was determined by Phenom ProX-SEM-EDS.

Table 2. Fractional thickness of Ag–Se film layers on nylon.

Layer	Fractional Thickness of the Layers, µm			
	Ag–Se-6/nylon	**Ag–Se-12/nylon**	**Ag–Se-24/nylon**	**Ag–Se-30/nylon**
Topmost (dark)	7.61–9.51	8.67–15.17	8.51–13.70	14.09–19.51
Intermediate (white)	7.61–13.31	8.67–10.14	5.15–7.87	4.34–9.76
Diffusion (grey)	7.61–9.51	8.67–13.00	8.52–11.61	8.67–10.64
Total	22.83–32.33	26.01–38.31	22.18–33.18	27.1–39.91

Table 3. Chemical composition from each fractional layer (spot 1, spot 2, and spot 3, as marked in Figure 3) of the Ag–Se-6/nylon nanocomposite obtained by EDS.

Spot	Atomic Concentrations, %						
	C	**O**	**N**	**S**	**Se**	**Ag**	**Ag/Se Concentration Ratio**
1	28.69	44.96	26.35	-	-	-	-
2	34.19	40.10	24.98	0.19	0.54	-	-
3	36.70	37.70	23.30	0.23	0.95	1.12	1.18

Table 4. Chemical composition from each fractional layer (spot 1, spot 2, and spot 3, as marked in Figure 3) of the Ag–Se-12/nylon nanocomposite obtained by EDS.

Spot	Atomic Concentrations, %						
	C	O	N	S	Se	Ag	Ag/Se Concentration Ratio
1	20.99	55.98	22.22	0.39	0.42	-	-
2	41.94	37.58	18.68	0.50	0.99	0.31	0.31
3	40.04	36.30	17.80	0.95	3.32	1.59	0.48

Table 5. Chemical composition from each fractional layer (spot 1, spot 2, and spot 3, as marked in Figure 3) of the Ag–Se-24/nylon nanocomposite obtained by EDS.

Spot	Atomic Concentrations, %						
	C	O	N	S	Se	Ag	Ag/Se Concentration Ratio
1	27.12	47.98	24.03	0.34	0.53	-	-
2	26.60	45.78	24.47	0.23	0.95	1.97	2.07
3	25.14	52.70	17.22	0.93	1.41	2.60	1.84

Table 6. Chemical composition from each fractional layer (spot 1, spot 2, and spot 3, as marked in Figure 3) of the Ag–Se-30/nylon nanocomposite obtained by EDS.

Spot	Atomic Concentrations, %						
	C	O	N	S	Se	Ag	Ag/Se Concentration Ratio
1	30.93	50.91	17.14	0.35	0.67	-	-
2	29.58	45.42	19.06	0.78	1.46	3.70	2.53
3	30.34	46.63	16.53	1.44	1.65	3.41	2.07

The results indicate that the silver, selenium, and sulphur atomic concentration of these fractional layers greatly depends on the selenium deposition time. From the depth profile EDS spectra data (Tables 3–6), it is clear that sulphur is present in all the three layers, thereby indicating that diffusion occurred during the a–Se/nylon template preparation. Likewise, in the first synthesis step, SeO_3^{2-}, SO_3^{2-}, or SO_4^{2-} ions as well as selenium nanoparticles penetrate into the polymer matrix until the concentration reaches an equilibrium value. The EDS spectra from the topmost (spot 3), intermediate (spot 2), and diffusion (spot 3) layers indicate non-homogeneous distribution of silver, selenium, and sulphur atomic concentration throughout its thickness. We note that, in all composites, silver was not detected in the diffusion layer (Tables 3–6). The calculated ratio f of the topmost layer was 1.17, 2.02, 1.84, and 2.06 for Ag–Se-6/nylon, Ag–Se-12/nylon, Ag–Se-24/nylon, and Ag–Se-30/nylon, respectively (Tables 3–6).

3.2. XRD Analysis

The crystallographic structure of the Ag–Se/nylon nanocomposites was studied by XRD analysis. Our previous XRD studies of the nylon matrix showed that the diffraction pattern features two dominant peaks at 2θ 20.1° and 23.5°, and the peak at 9.4° of lower intensity [29]. As the intensities of nylon XRD peaks sharply exceeded the XRD patterns of the obtained composites, the diffractograms are given in the 30–65° 2θ angular interval. The experimental data were interpreted by using the standard JCPDS cards and the data available in the literature [5,30]. Analysis results are presented in Figure 4.

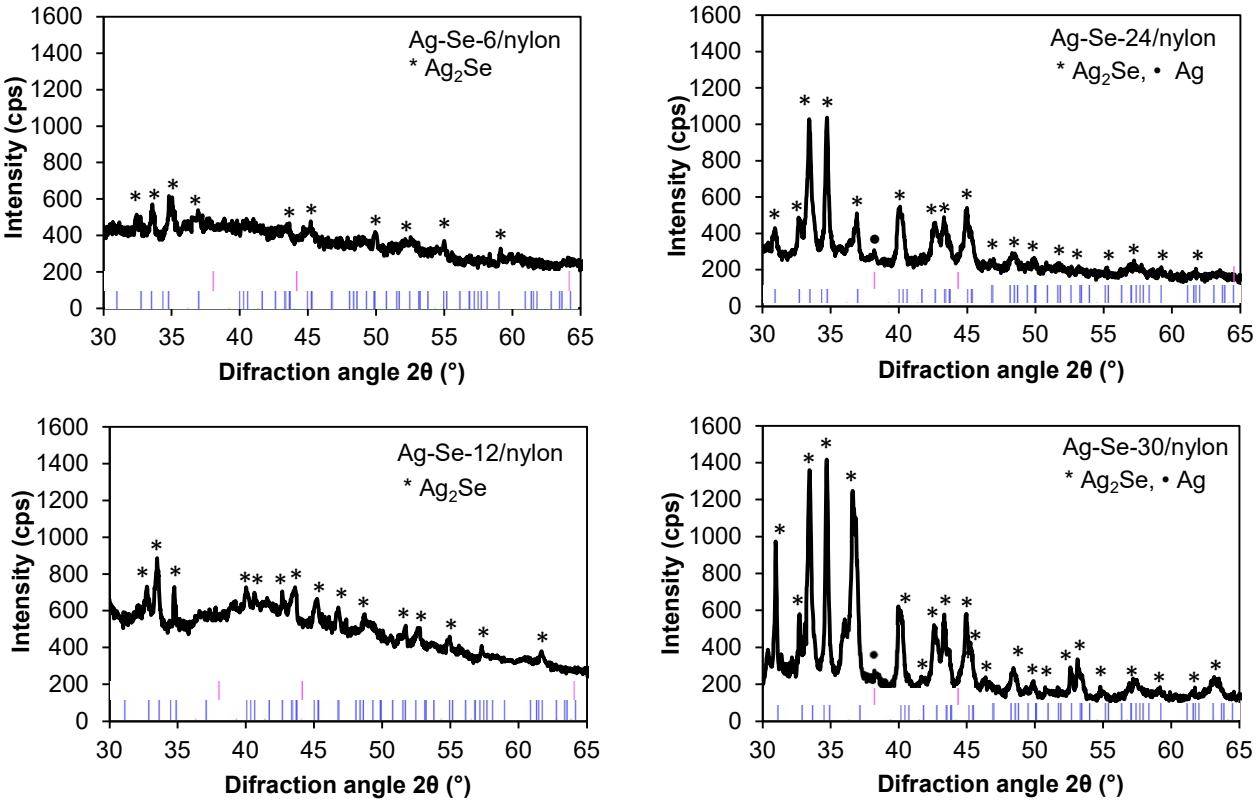

Figure 4. XRD patterns of Ag–Se films on the nylon surface. The black lines are the experimental patterns, and the pink and blue lines label the peaks from Ag (04-003-1472 (Calc., Intensity: 36.0%)) and Ag_2Se (01-071-2410 (Calc., Intensity: 91.0%)), respectively.

The Ag–Se-6/nylon nanocomposite showed diffraction peaks corresponding to the orthorhombic naumannite phase of Ag_2Se (JCPDS # 01-071-2410, λ = 0.15406 nm). As observed from the pattern, the predominant (121) peak of the orthorhombic system represents a preferred orientation along this plane. The identified peak positions coincide well with the ones reported in literature for Ag_2Se nanowires [5] and nanoparticles [30]. With a further increase in the selenium deposition time (Figure 4 Ag–Se-12/nylon sample), the intensity of the reflection (112) line increased, whereas the number of new peaks corresponding to the silver selenide phase rose. The diffractogram of the Ag–Se-24/nylon nanocomposite showed two sharp lines of nearly equal intensity along (112) and (121) planes, respectively. The orientation along (121) plane became predominant in the Ag–Se-30/nylon nanocomposite. In the Ag–Se-24/nylon and Ag–Se-30/nylon samples diffractograms, the metallic Ag phase (JCPDS # 04-003-1472, λ = 0.15406 nm) was also detected. Usually, the metallic Ag structure is depicted by a sharp XRD peak at 2θ 38.12° corresponding to a preferential (111) texture. Together with the Ag_2Se phase, a minor amount of elemental selenium may remain not reacted in the deposited film. At room temperature, deposited Se is amorphous and not detected by XRD. Since the Ag_2SeO_3, Ag_2SO_3, and Ag_2SO_4 phases were not found in Ag–Se/nylon nanocomposites, it could be assumed that the SeO_3^{2-}, SO_3^{2-}, and SO_4^{2-} ions diffused out from the a–Se/nylon template, and reacted with the silver ions to produce these compounds in solution nearby the a–Se/nylon template region. In the other case, the by-products of this reaction, due to high solubility, were removed from sample surface by rinsing with excess hot water before XRD analysis.

3.3. AFM Analysis

The 2D and 3D AFM images for scanning areas of 30 × 30 μm^2 are presented in Figure 5.

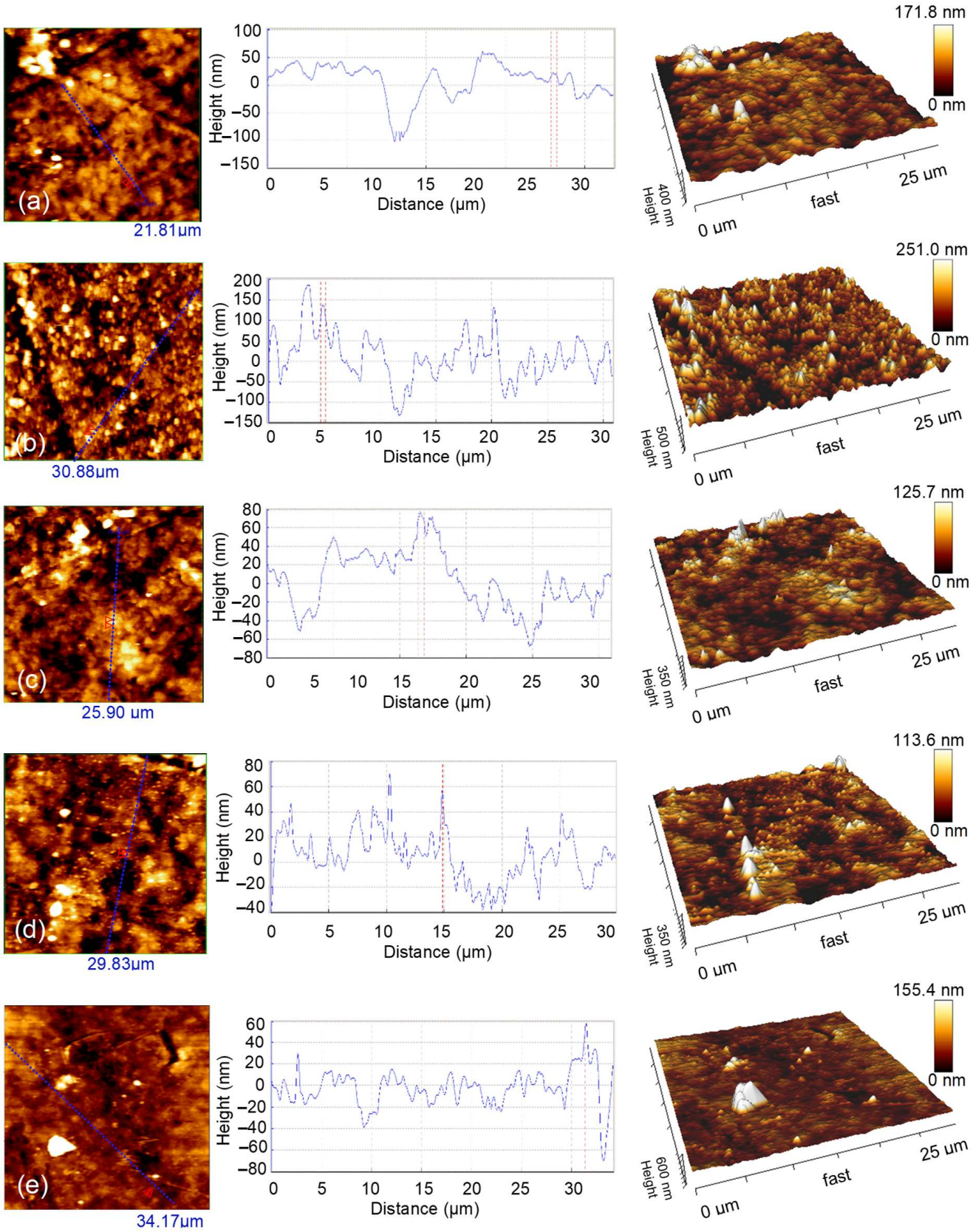

Figure 5. AFM views (left—2D views; center—profile; right—3D views) of (**a**) uncoated nylon, (**b**) Ag–Se-6/nylon, (**c**) Ag–Se-12/nylon, (**d**) Ag–Se-24/nylon, (**e**) Ag–Se-30/nylon.

The experimental results evidently indicate that the surface topography of the Ag–Se/nylon nanocomposites strongly depends on the selenium deposition time. As it can be seen, the uncoated nylon showed a morphology composed of some bulges, sags, and pores (Figure 5a). These structures of various scales also existed in the Ag–Se-6/nylon sample, and were distributed unevenly in some ranges (Figure 5b). In addition, these features possess different irregular shapes, sizes, and separations. With a further increase in the selenium deposition time (Figure 5c–e), we observed the appearance of particles agglomerates, which form separated islands. There are also various darker areas (spots and channels) filled with the several smaller grains, indicating the non-uniform growth of layers across film thickness. Alternatively, these spots and channels may represent the holes and cracks extracting down to the depth. In addition, randomly distributed pyramidal-like structures were also visible. It is difficult to notice a significant relationship between the size, shape, and the number density of morphological defects and the selenium deposition time. An examination of all AFM images indicates that the smallest number density of morphological defects is in the Ag–Se-30/nylon nanocomposite. The roughness of the composite surface strongly affects the reflectance of light and is crucial for materials application in the optoelectronic devices. The topographical parameters elucidated by using AFM analysis are gathered in Table 7.

Table 7. Surface topographical parameters average height (Z_{mean}), average roughness (R_a), root-mean-square surface roughness (R_q), and peak-to-valley roughness (R_t) obtained by AFM analysis.

Sample	Z_{mean} (nm)	R_a (nm)	R_q (nm)	R_t (nm)
Uncoated nylon	171.8	28.22	39.06	429.0
Ag–Se-6/nylon	251.0	43.19	57.04	547.0
Ag–Se-12/nylon	125.7	20.67	28.57	350.9
Ag–Se-24/nylon	113.6	18.53	25.82	369.2
Ag–Se-30/nylon	155.4	17.54	35.33	607.6

The root-mean-square surface roughness (R_q) of the obtained composites decreased with an increase of the selenium deposition time from 12 to 24 h, and, in Ag–Se-12/nylon and Ag–Se-24/nylon nanocomposites, it was lower than that of uncoated nylon, but it increased with the prolongation of the selenium deposition time up to 30 h (Table 7). The variation trend in the height and roughness values may be related to the deviation of the films composition from the stoichiometric ratio of Ag and Se (Tables 1 and 3–6) and variation in the thickness of the Ag_2Se film (Table 2). Additionally, the mobility and diffusion of the SO_3^{2-} and SeO_3^{2-} ions into the sub-surface space of nylon may enhance or inhibit the grain growth and hence affect the surface morphology (R_q) and roughness of the deposited films. The (R_q) obtained values of 25.82–57.04 nm reasonably suggest that the surface morphology is responsible for the relatively high refractive indices of the Ag–Se/nylon nanocomposites (as discussed in the section on UV-Vis analysis). The height distribution function gives the number of times that regions of a constant height occur in the morphology of the film [21]. Figure 6 shows a relatively homogeneous particle height distribution for the Ag–Se/nylon nanocomposites. Kurtosis (R_{Ku}) and skewness (R_{sk}) parameters equaled 3.1 $\pm$ 0.1 and 0.2 $\pm$ 0.05, respectively, suggesting a quasi-symmetric Gaussian distribution.

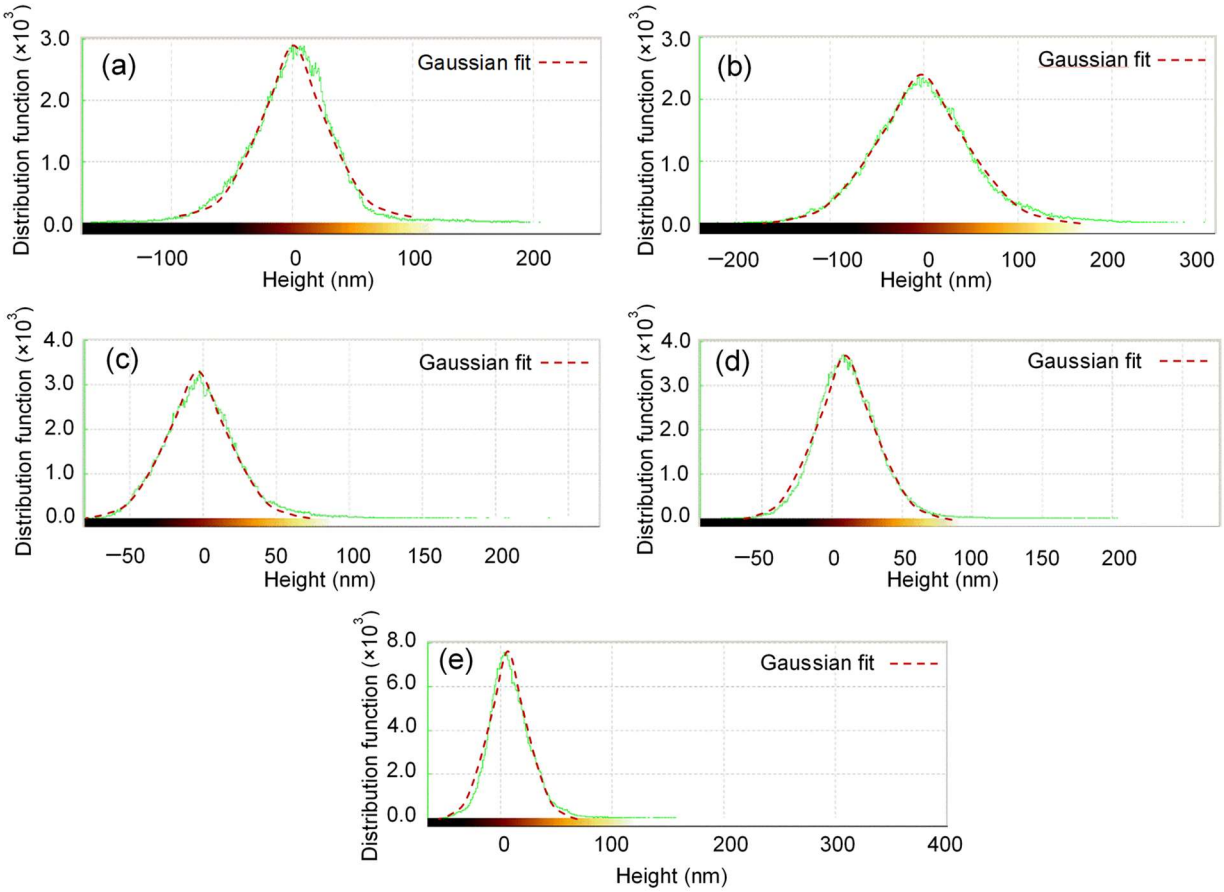

Figure 6. Histogram of the height distribution function in AFM images of (**a**) uncoated nylon, (**b**) Ag–Se-6/nylon, (**c**) Ag–Se-12/nylon, (**d**) Ag–Se-24/nylon, (**e**) Ag–Se-30/nylon samples.

3.4. UV-Vis Analysis

In the spectrum of the Ag–Se-6/nylon sample (Figure 7), the maximum absorption peak was located at 477 nm, accompanied by a shoulder peak at 584 nm.

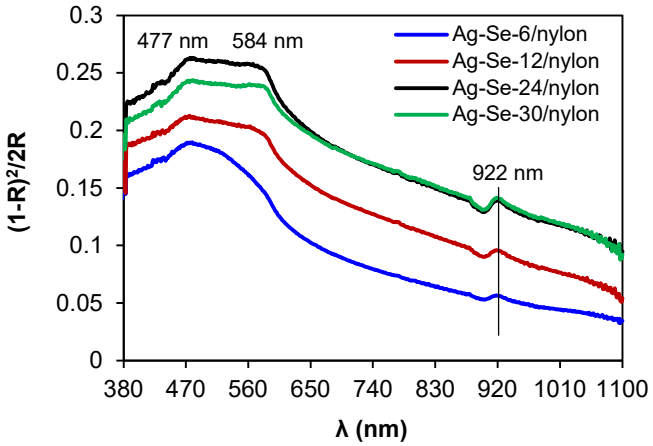

Figure 7. Optical absorption spectra of Ag–Se/nylon nanocomposites.

It is obvious that both absorption features did not shift with the selenium deposition time, but they were just subjected to an increase in their intensities. The literature reports wide absorption bands in the region between 300 and 600 nm for Ag_2Se nanoparticles [31]. In the wavelength range higher than 620 nm (near the infrared spectral range), the absorbance monotonically decreased. The peak at 922 nm possibly arises from the absorption

by some large coalescing aggregates. The Kubelka–Munk method was applied to determine an optical band gap (E_{op}). The E_{op} and the reflectance are interrelated by the equations given below [25,26]: This is example 1 of an equation:

$$F{\cdot}(R) = \frac{(1-R)^2}{2{\cdot}R}, \tag{9}$$

$$hvF \sim (hv - E_{op})^n, \tag{10}$$

where F—the Kubelka–Munk function, R—the reflectance, hv—the photon energy, and E_{op} is the optical band gap, n is a constant characterising the transition mode, $n = 1/2$ or 2 are for the allowed direct or indirect transitions, respectively.

The variation of $(hvF)^2$ versus hv for each composite is shown in Figure 8. The linear part in the higher energy region confirms the allowed direct transition mode. The intersection of a long straight-line part with the photon energy axis depicts E_{op} value. The obtained values were 1.86 eV, 1.76 eV, 1.70 eV, and 1.68 eV for Ag–Se-6/nylon, Ag–Se-12/nylon, Ag–Se-24/nylon and Ag–Se-30/nylon nanocomposites, respectively. The similar values were reported in ref. [10]. The red shift of E_{op} values with an increasing of selenium deposition time can be related to the polycrystalline structure of Ag_2Se and a relatively high surface roughness (Table 7). Additionally, the structural defects generated from the dispersed selenium nanoparticles and adsorbed SeO_3^{2-}, SO_3^{2-}, or SO_4^{2-} ions in the composites can also contribute to the band gap value [32]. The Ag_2Se had a narrow band gap (~0.15 eV) in the bulk case at room temperature [33]. The higher E_{op} values as compared with that of bulk Ag_2Se suggest that the particle sizes were within the quantum confinement regime [34].

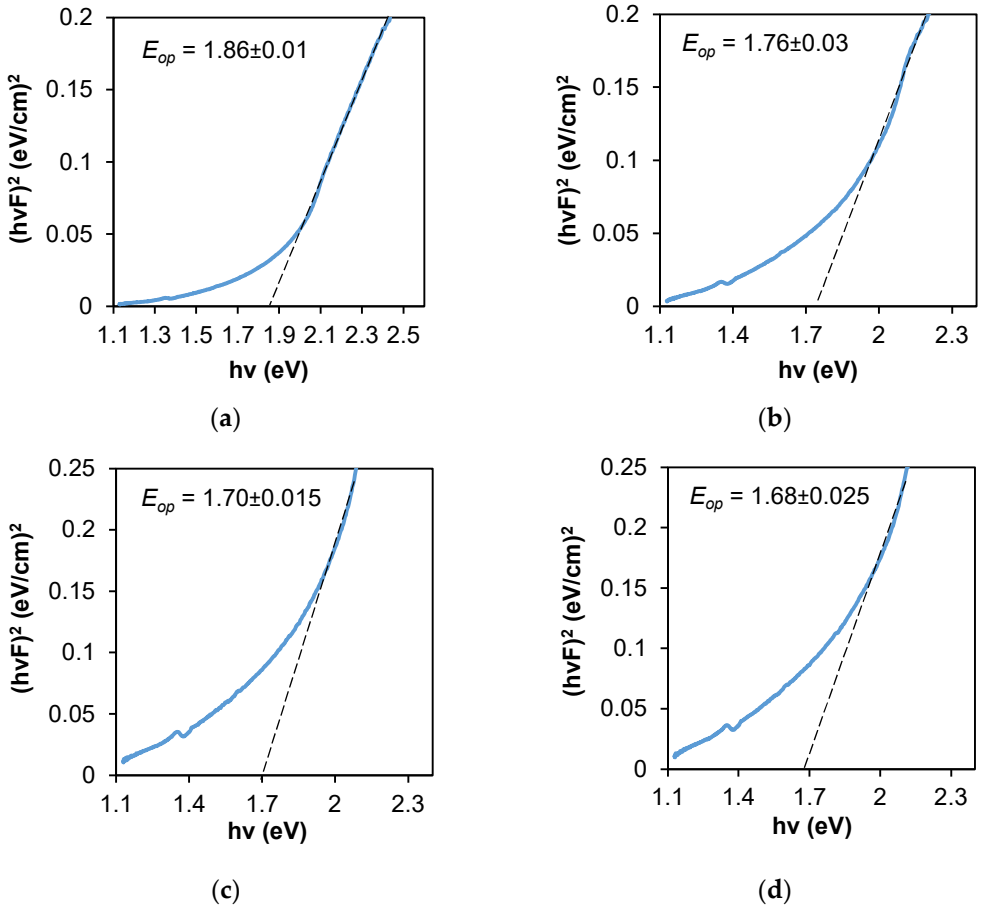

Figure 8. Optical band gap determination from diffuse reflectance spectra by the Kubelka–Munk method: (**a**) Ag–Se-6/nylon; (**b**) Ag–Se-12/nylon; (**c**) Ag–Se-24/nylon; (**d**) Ag–Se-30/nylon samples.

The refractive index difference of constituent materials causes a significant light scattering as well as a loss of transparency in organic-inorganic composites [35]. The following equation was applied to calculate the refractive indices (n): [36,37]:

$$n = \frac{-(R+1) \pm 2\sqrt{R}}{R-1}. \quad (11)$$

The spectral behaviour of indices (Figure 9) showed a very complex character.

In the spectral region between 380 and 477 nm, the refractive indices of all the investigated Ag–Se/nylon nanocomposites illustrated a slow decrease, which can be explained by a single oscillator model [36]. As we can observe, the refractive indices of the Ag–Se-6/nylon nanocomposite increased in the spectral interval from 477 nm to 584 nm, while, for the three other nanocomposites (Ag–Se-12/nylon, Ag–Se-24/nylon and Ag–Se-30/nylon), it remained nearly constant (the plateau region). In the region at λ > 590 nm, the refractive indices monotonically increased showing an anomalous dispersion [38]. As discussed above, various sub-micron structures, particles and agglomerates covered the nylon surface (Figure 2). These structural elements can also contribute to the anomalous dispersion [39]. At the same time, the refractive indices depend on the selenium deposition time. Specifically, Ag–Se-6/nylon nanocomposite possesses the ultra-high refractive index as compared with other samples (Figure 9). For example, the values of refractive indices for Ag–Se-6/nylon and Ag–Se-30/nylon nanocomposites at λ = 800 nm were 3.68 and 1.98, respectively and coincide well with those reported in ref. [40]. Finally, we must note that the investigated composites possessed high refractive index values. Consequently, they are promising for the development of efficient flat waveguide components and anti-reflective coatings.

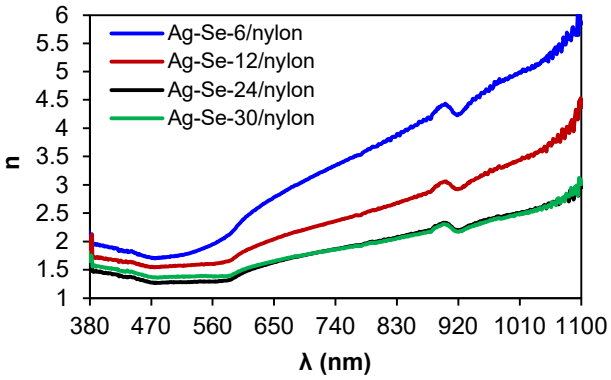

Figure 9. Variation of refractive indices of Ag–Se/nylon nanocomposites on wavelength.

4. Conclusions

Compact multilayer Ag–Se/nylon semiconductor nanocomposites were synthesised via a template-engaged reaction, which could convert the a–Se layer on nylon into an Ag–Se film. The obtained results imply that the surface morphology, and elemental and phase composition of Ag–Se/nylon nanocomposites as well as their optical properties were highly sensitive to the selenium deposition time on nylon. Scanning electron microscope (SEM) analysis confirmed the development of a very complex surface composed of pyramidal-like sub-micron structures, agglomerates, and grid-like structures. Energy dispersive spectroscopy (EDS) of large areas (10 × 11.5 μm^2) proved the presence of carbon, oxygen, nitrogen, sulphur, selenium, and silver. The higher content of oxygen was observed in all the obtained composites as compared with that of an uncoated nylon sample, which distinctly suggests the presence of oxygen containing ions, such as SeO_3^{2-}, SO_3^{2-}, or SO_4^{2-}. SEM/EDS cross-sectional analysis proves the multilayer character of the composite with a different individual elemental composition in each layer. X-ray diffraction analysis indicates that Ag–Se/nylon nanocomposites obtained at shorter selenium deposition times exist as polycrystalline naumannite Ag_2Se; composites obtained at longer selenium deposition times exist as a mixed-phase material composed of Ag_2Se and metallic Ag. The RMS

value obtained from the atomic force microscopy varied from 25.82 nm to 57.04 nm. The direct optical band gap (E_{op}) was found to be 1.68–1.86 eV. Ag–Se/nylon nanocomposites exhibited high refractive indices in the visible and near infrared region. The presented results are promising for the optimisation of Ag_2Se/nylon nanocomposite fabrication process, which is one of the most important components in flexible electronics.

Author Contributions: Conceptualisation, V.K. and N.D.; methodology, V.K.; software, V.K.; validation, N.D., V.K. and H.M.; formal analysis, N.D.; investigation, H.M.; resources, N.D.; data curation, N.D.; writing—original draft preparation, V.K.; writing—review and editing, N.D.; visualisation, H.M.; supervision, V.K.; project administration, V.K.; funding acquisition, V.K. All authors have read and agreed to the published version of the manuscript.

Funding: This research was funded by the Doctoral Fund of Kaunas University of Technology No. A-410, approved 26 June 2019.

Institutional Review Board Statement: Not applicable.

Informed Consent Statement: Not applicable.

Data Availability Statement: Data is contained within the article.

Conflicts of Interest: The authors declare no conflict of interest.

References

1. Li, Q.; Zanelli, A. A review on fabrication and applications of textile envelope integrated flexible photovoltaic systems. *Renew. Sustain. Energy Rev.* **2021**, *139*, 110678. [CrossRef]
2. Saveleva, M.S.; Eftekhari, K.; Abalymov, A.; Douglas, T.E.L.; Volodkin, D.; Parakhonskiy, B.V.; Skirtach, A.G. Hierarchy of Hybrid Materials—The Place of Inorganics-in-Organics in it, Their Composition and Applications. *Front. Chem.* **2019**, *7*, 179. [CrossRef] [PubMed]
3. Hilal, H.S.; Zyoud, A.; Helal, M.H.S.; Bsharat, H.; Helal, H.H.; Ali, C. Effects of annealing temperature and cooling rate on photo-electrochemical performance of pristine polycrystalline metal-chalcogenide film electrodes. *Sol. Energy* **2019**, *183*, 704–715. [CrossRef]
4. Mlambo, M.; Moloto, M.J.; Moloto, N.; Mdluli, P.S. Influence of temperature and precursor concentration on the synthesis of HDA-capped Ag2Se nanoparticles. *Mater. Res. Bull.* **2013**, *48*, 2196–2200. [CrossRef]
5. Gates, B.; Mayers, B.; Wu, Y.; Sun, Y.; Cattle, B.; Yang, P.; Xia, Y. Synthesis and Characterization of Crystalline Ag $_2$ Se Nanowires Through a Template-Engaged Reaction at Room Temperature. *Adv. Funct. Mater.* **2002**, *12*, 679–686. [CrossRef]
6. Husmann, A.; Betts, J.B.; Boebinger, G.S.; Migliori, A.; Rosenbaum, T.F.; Saboungi, M.-L. Megagauss sensors. *Nature* **2002**, *417*, 421–424. [CrossRef] [PubMed]
7. Ding, Y.; Qiu, Y.; Cai, K.; Yao, Q.; Chen, S.; Chen, L.; He, J. High performance n-type Ag2Se film on nylon membrane for flexible thermoelectric power generator. *Nat. Commun.* **2019**, *10*, 841. [CrossRef]
8. Schoen, D.T.; Xie, C.; Cui, Y. Electrical Switching and Phase Transformation in Silver Selenide Nanowires. *J. Am. Chem. Soc.* **2007**, *129*, 4116–4117. [CrossRef]
9. Kobayashi, M. Review on structural and dynamical properties of silver chalcogenides. *Solid State Ionics* **1990**, *39*, 121–149. [CrossRef]
10. Pejova, B.; Najdoski, M.; Grozdanov, I.; Dey, S.K. Chemical bath deposition of nanocrystalline (111) textured Ag2Se thin films. *Mater. Lett.* **2000**, *43*, 269–273. [CrossRef]
11. Wu, M.; Cai, K.; Li, X.; Li, Y.; Liu, Y.; Lu, Y.; Wang, Z.; Zhao, W.; Wei, P. Ultraflexible and high-thermoelectric-performance sulfur-doped Ag_2Se film on nylon for power generators. *ACS Appl. Mater. Interfaces* **2022**, *14*, 4307–4315. [CrossRef]
12. Gao, Q.; Wang, W.; Lu, Y.; Cai, K.; Li, Y.; Wang, Z.; Wu, M.; Huang, C.; He, J. High power factor Ag/Ag_2Se composite films for flexible thermoelectric generators. *ACS Appl. Mater. Interfaces* **2021**, *13*, 14327–14333. [CrossRef]
13. Zhang, S.-Y.; Fang, C.-X.; Wei, W.; Jin, B.-K.; Tian, Y.-P.; Shen, Y.-H.; Yang, J.-X.; Gao, H.-W. Synthesis and Electrochemical Behavior of Crystalline Ag_2Se Nanotubes. *J. Phys. Chem. C* **2007**, *111*, 4168–4174. [CrossRef]
14. Jiang, Z.-Y.; Xie, Z.-X.; Zhang, X.-H.; Huang, R.-B.; Zheng, L.-S. Conversion of Se nanowires to Se/Ag2Se nanocables and Ag2Se nanotubes. *Chem. Phys. Lett.* **2003**, *378*, 313–316. [CrossRef]
15. Gates, B.; Wu, Y.; Yin, Y.; Yang, P.; Xia, Y. Single-Crystalline Nanowires of Ag_2Se Can Be Synthesized by Templating against Nanowires of Trigonal Se. *J. Am. Chem. Soc.* **2001**, *123*, 11500–11501. [CrossRef]
16. Greenwood, N.N.; Earnshaw, A. (Eds.). Selenium, Tellurium and Polonium. In *Chemistry of the Elements*, 2nd ed.; Elsevier Ltd., Butterworth-Heinemann: Oxford, UK, 1997; Volume 16, pp. 747–788. [CrossRef]
17. Sukyte, J.; Ivanauskas, R.; Ancutiene, I. Comparative study of selenopolythionic acids $H_2Se_nS_2O_6$ as precursors for formation of chalcogenides layers. *Chalcogenide Lett.* **2015**, *12*, 569–578.
18. Luo, Y.-R. *Comprehensive Handbook of Chemical Bond Energies*, 1st ed.; CRC Press: Boca Raton, FL, USA, 2007; p. 1688. [CrossRef]

19. Olin, Å.; Noläng, B.; Osadchii, E.G.; Öhman, L.-O.; Rosén, E. *Chemical Thermodynamics of Selenium*, 1st ed.; Elsevier Science: Amsterdam, The Netherlands, 2005; p. 894. Available online: https://www.oecd-nea.org/dbtdb/pubs/vol7-selenium.pdf (accessed on 14 April 2022).
20. Feng, S.; Xu, R. New Materials in Hydrothermal Synthesis. *Acc. Chem. Res.* **2001**, *34*, 239–247. [CrossRef]
21. Mohanty, B.C.; Murty, B.S.; Vijayan, V.; Kasiviswanathan, S. Atomic force microscopy study of thermal stability of silver selenide thin films grown on silicon. *Appl. Surf. Sci.* **2006**, *252*, 7975–7982. [CrossRef]
22. Saito, Y.; Sato, M.; Shiojiri, M. Orientation in Ag2Se polymorphic films produced by the reaction of silver films with selenium. *Thin Solid Films* **1981**, *79*, 257–266. [CrossRef]
23. Krylova, V.; Dukštienė, N. The structure of PA-Se-S-Cd composite materials probed with FTIR spectroscopy. *Appl. Surf. Sci.* **2019**, *470*, 462–471. [CrossRef]
24. Mokgalapa, N.M.; Ghosh, T.K.; Tompson, R.V.; Loyalka, S.K. Adhesion Force between a Silver Particle and Haynes 230: Role of Surface Conditions. *Nucl. Technol.* **2016**, *194*, 353–368. [CrossRef]
25. López, R.; Gómez, R. Band-gap energy estimation from diffuse reflectance measurements on sol–gel and commercial TiO2: A comparative study. *J. Sol-Gel Sci. Technol.* **2012**, *61*, 1–7. [CrossRef]
26. Nasr, M.; Viter, R.; Eid, C.; Warmont, F.; Habchi, R.; Miele, P.; Bechelany, M. Synthesis of novel ZnO/$ZnAl_2O_4$ multi co-centric nanotubes and their long-term stability in photocatalytic application. *RSC Adv.* **2016**, *6*, 103692–103699. [CrossRef]
27. Kienle, L.; Duppel, V.; Mogwitz, B.; Janek, J.; Kreutzbruck, M.V.; Leineweber, A.; Simon, A. Synthesis–Real Structure–Property: The Showcase of Silver-Rich Ag2Se. *Cryst. Growth Des.* **2011**, *11*, 2412–2421. [CrossRef]
28. Beck, G.; Janek, J. Negative and linear positive magnetoresistance effect in silver-rich silver selenide. *J. Solid State Sci.* **2008**, *10*, 776–789. [CrossRef]
29. Krylova, V.; Dukstienė, N.; Žalenkienė, S.; Baltrusaitis, J. Chemical and structural changes in polyamide based organic–inorganic hybrid materials upon incorporation of SeS2O62−precursor. *Appl. Surf. Sci.* **2017**, *392*, 634–641. [CrossRef]
30. Ayele, D.W. A facile one-pot synthesis and characterization of Ag_2Se nanoparticles at low temperature. *Egypt. J. Basic Appl. Sci.* **2016**, *3*, 149–154. [CrossRef]
31. Delgado-Beleño, Y.; Martinez-Nuñez, C.E.; Cortez-Valadez, M.; Flores-López, N.S.; Flores-Acosta, M. Optical properties of silver, silver sulfide and silver selenide nanoparticles and antibacterial applications. *Mater. Res. Bull.* **2018**, *99*, 385–392. [CrossRef]
32. Abdelrazek, E.M.; Abdelghany, A.M.; Badr, S.I.; Morsi, M.A. Structural, optical, morphological and thermal properties of PEO/PVP blend containing different concentrations of biosynthesized Au nanoparticles. *J. Mater. Res. Technol.* **2018**, *7*, 419–431. [CrossRef]
33. Zhu, C.-N.; Chen, G.; Tian, Z.-Q.; Wang, W.; Zhong, W.-Q.; Li, Z.; Zhang, Z.-L.; Pang, D.-W. Near-Infrared Fluorescent Ag_2Se-Cetuximab Nanoprobes for Targeted Imaging and Therapy of Cancer. *Small* **2017**, *13*, 1602309. [CrossRef]
34. Anthony, S.P. Synthesis of Ag2S and Ag2Se nanoparticles in self assembled block copolymer micelles and nano-arrays fabrication. *Mater. Lett.* **2009**, *63*, 773–776. [CrossRef]
35. Loste, J.; Lopez-Cuesta, J.-M.; Billon, L.; Garay, H.; Save, M. Transparent polymer nanocomposites: An overview on their synthesis and advanced properties. *Prog. Polym. Sci.* **2019**, *89*, 133–158. [CrossRef]
36. Rashad, M. Tuning optical properties of polyvinyl alcohol doped with different metal oxide nanoparticles. *Opt. Mater.* **2020**, *105*, 109857. [CrossRef]
37. Jatautė, L.; Krylova, V.; Dukštienė, N.; Lelis, M.; Tučkutė, S. Ag-In-Se films on flexible architectural textiles as efficient material for optoelectronics applications: A preliminary study. *Thin Solid Films* **2021**, *721*, 138566. [CrossRef]
38. Raj, K.R.; Murugakoothan, P. Studies on the optical and mechanical properties of non-linear optical 3-aminophenol orthophosphoric acid (3-amphph) single crystal. *Optik* **2012**, *123*, 1082–1086. [CrossRef]
39. Beaglehole, D.; Hunderi, O. Study of the Interaction of Light with Rough Metal Surfaces. I. Experiment. *Phys. Rev. B* **1970**, *2*, 309–321. [CrossRef]
40. Pandiaraman, M.; Soundararajan, N.; Vijayan, C.; Kumar, C.; Ganesan, R. Spectroscopic studies on silver selenide thin films. *J. Ovonic Res.* **2010**, *6*, 285–295.